RSC Advances

PAPER

View Article Online
View Journal | View Issue

Check for updates

Cite this: *RSC Adv.*, 2022, **12**, 24055

Quantitative prediction of CeO_2 and $LaAlO_3$ infrared spectra based on first-principles calculations

Guangpu Luo,[a] Wenyue Zhao,[ab] Hongbo Guo*[cd] and Shengkai Gong*[a]

Oxide crystals with specific infrared spectra are widely used in the optical energy industry. Conventional density functional theory calculations reveal various properties of oxide crystals, including their electronic band structure, electronic density of states, vibrational modes, phonon band structure, and phonon density of states, but only provide qualitative analyses of infrared spectra. Herein, we provide a theoretical approach to analyzing how the basic mechanisms of infrared absorption are affected by the above properties and then predicting quantitatively the infrared spectra. The derivation and details of this method are clarified, and the CeO_2 and $LaAlO_3$ infrared spectra are finally calculated through an application. The calculated infrared properties are in good agreement with previously reported experiments, demonstrating the accuracy of our method. This study provides a less expensive approach to identifying the infrared spectra of oxide crystals through the use of theoretical calculations and is potentially applicable in the optical energy industry, improving the efficiency by which appropriate materials can be selected.

Received 8th June 2022
Accepted 18th July 2022

DOI: 10.1039/d2ra03539a

rsc.li/rsc-advances

Open Access Article. Published on 24 August 2022. Downloaded on 1/31/2026 1:38:06 AM.
This article is licensed under a Creative Commons Attribution-NonCommercial 3.0 Unported Licence.

1 Introduction

Oxide crystals with specific infrared spectra play a key role in the optical energy industry. Solar panels better utilize materials that effectively absorb visible and near-infrared light and rarely emit radiation in the mid-infrared or far-infrared range. The radiative cooling surface requires high emissivity in the 3–5 μm and 8–14 μm range, as infrared radiation in this range can easily travel in air. Moreover, an energy-saving coating is required to absorb the majority of thermal radiation from the high-temperature oven. According to Wien's law, an oven operated at 600–1200 °C has a radiation peak at 2.0–3.5 μm. Absorption and radiation share similar mechanisms as forward and reverse processes. The discussion below focuses on infrared absorption but is also applicable to infrared radiation. The growing industry motivates research in the discovery of suitable appropriate infrared materials. These materials include oxide crystals, which have attracted widespread interest due to their ease of synthesis and stability at high temperatures.

In recent years, a great amount of cost has been paid towards investigating the infrared properties of various materials by experimentation. Alternatively, theoretical analysis can reduce these costs. Since 1965,[1,2] first-principles calculations based on density functional theory (DFT) have undergone rapid development. These first-principles calculations have been applied in multiple industries with desirable results. DFT calculations used in the investigation of oxide crystals provide properties such as electronic band structure, electronic density of states (DOS), molecular vibrational modes, phonon band structure, and phonon DOS. However, conventional DFT analyses only provide qualitative results of the infrared spectra. When the electronic band structure and the electronic DOS were investigated, the narrow band gap and high density of the free carriers indicated strong infrared absorption. All modes that may influence infrared absorption were provided when the molecular vibrational modes were investigated. These molecular vibrational modes are compared with the experimental infrared spectra to determine which were infrared active. In addition, the phonons on transverse optical branches were found to affect infrared absorption when the phonon band structure and phonon DOS were investigated. A theoretical method combined with first-principles calculations and basic mechanisms of infrared absorption is presented further in the paper, which provides quantitative predictions of the infrared spectra of oxide crystals.

Four basic mechanisms result in infrared absorption within the wavelength range of 0.3–14.0 μm: intrinsic absorption, exciton absorption, free-carrier absorption, and lattice absorption.[3] For semiconductors at temperatures lower than −200 °C, an exciton absorption spectrum is rarely found near an intrinsic absorption spectrum. Considering the industrial requirements,

[a]*Research Institute for Frontier Science, Beihang University, Beijing 100191, China. E-mail: gongsk@buaa.edu.cn*

[b]*Key Laboratory of Aerospace Materials and Performance (Ministry of Education), Beihang University, Beijing 100191, China*

[c]*School of Materials Science and Engineering, Beihang University, Beijing 100191, China. E-mail: guo.hongbo@buaa.edu.cn*

[d]*Key Laboratory of High-Temperature Structural Materials and Protective Coatings (Ministry of Industry and Information Technology), Beihang University, Beijing 100191, China*

© 2022 The Author(s). Published by the Royal Society of Chemistry

Open Access Article. Published on 24 August 2022. Downloaded on 1/31/2026 1:38:06 AM.
This article is licensed under a Creative Commons Attribution-NonCommercial 3.0 Unported Licence.

only the infrared spectra of oxide crystals at 0–1200 °C were investigated and exciton absorption was considered negligible. In our method, intrinsic absorption was obtained from the quantitative analyses of the electronic band structure and the electronic DOS. Free-carrier absorption was affected by phonons, electronic band structure, and electronic DOS, while lattice absorption consists of molecular vibrational absorption and phonon absorption. Compared with conventional analyses, our method adds a step to identify the infrared activity of the molecular vibrational modes and quantitatively predicts the infrared absorption peaks and their amplitudes.

The derivation and details of our method are introduced in the Computational methodology section. Then, the infrared spectra of CeO_2 and $LaAlO_3$ as calculated by our method are described in the Result and discussion section. The calculated spectra are in good agreement with previously reported experimental results. Our method accurately provides the infrared properties of oxide crystals without the dependence of experiments, with promising applicability in the efficient selection of oxide crystals with high efficiency and related research.

2 Computational methodology

The DFT-based first-principles calculations were performed using the Vienna *Ab initio* Simulation Package (VASP).[4–8] In all calculations, plane-wave pseudopotential approximation was applied with the generalized gradient approximation (GGA) Perdew–Burke–Ernzerhof (PBE) exchange functional.[9–11] The properties of the phonons were calculated by VASP and using PHONOPY code based on the finite displacement method and the supercell approach.[12,13] The Hessian matrix was determined with density-functional perturbation theory (DFPT).

Considering practical applications, we only considered an infrared spectrum with a wavelength range of 0.3–14.0 μm. Most solar energy is distributed around 0.5 μm, the wavelengths of the thermal radiation peaks of objects at 0–1200 °C range from 2.0 to 10.6 μm, and infrared radiation can travel in air for long distances when its wavelength is 3–5 μm or 8–14 μm. Thus, a spectrum with a wavelength range of 0.3–14.0 μm covers all the necessary infrared radiations and absorptions.

2.1 Conventional density functional theory (DFT) results of ABO

Assume that there exists a simple hypothetical oxide crystal ABO whose unit cell is a cube (Fig. 1).

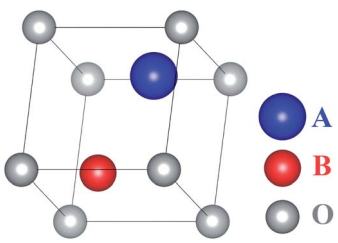

Fig. 1 Molecular geometry of the hypothetical oxide crystal ABO.

The first-principles calculations provide the electronic DOS and electronic band structure indicated in Fig. 2, the molecular vibrational modes are depicted in Fig. 3, and the band DOS and band structure of the phonons are shown in Fig. 4.

It is assumed that ABO has two molecular vibrational modes with eigenvalues of 1200 and 700 cm^{-1}, respectively.

2.2 Theoretical infrared spectra of ABO

Our method predicts the infrared spectra based on the results of the calculations shown above. The method individually considers the influence of the basic mechanisms of infrared absorption (*i.e.*, intrinsic absorption, free-carrier absorption, and lattice absorption).

2.2.1 Intrinsic absorption. Intrinsic absorptions take place when the photons are absorbed by carriers (electrons or holes) and transitions occur between different bands.

To simplify the analysis, we considered only two transitions that would lead to intrinsic absorptions. The intrinsic absorptions of ABO are depicted in Fig. 5. The valence band is located below the Fermi level and is fully occupied by valence electrons, while the conduction band is located above the Fermi level and

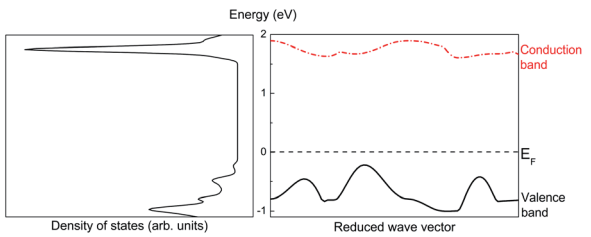

Fig. 2 Density of states (left) and band structure (right) of ABO.

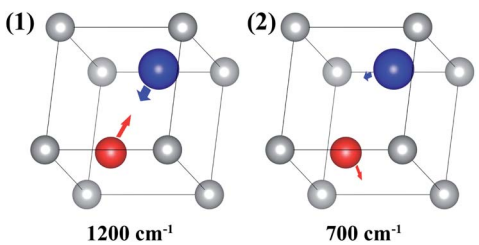

Fig. 3 Two molecular vibrational modes of ABO; the vectors represent the eigenvector of the vibrational modes.

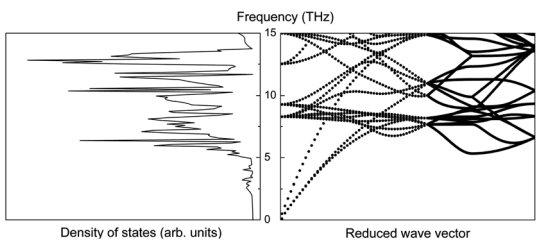

Fig. 4 Phonon density of states (left) and phonon band structure (right) of ABO.

© 2022 The Author(s). Published by the Royal Society of Chemistry

Open Access Article. Published on 24 August 2022. Downloaded on 1/31/2026 1:38:06 AM.
This article is licensed under a Creative Commons Attribution-NonCommercial 3.0 Unported Licence.

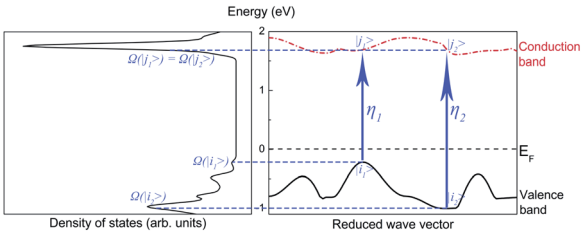

Fig. 5 Intrinsic absorptions of ABO.

is not occupied. If a photon is absorbed by an electron occupied at state $|i\rangle$ on the valence band, a transition occurs, and the electron occupies another state $|j\rangle$ on the conduction band. Considering that a photon transfers at a momentum negligibly small relative to the size of the Brillouin zone, the conservation of momentum leads to $k_i = k_j$. This equation indicates a "vertical transition", which is also known as a "direct transition". Direct transitions are the primary process since indirect transitions occur with much smaller probabilities. Energy is conserved *via* the transition, so $E_{\text{photon}} = E_\eta = E_j - E_i$.

Assuming that η_n represents a direct transition from a state $|i_n\rangle$ at the valence band to a state $|j_n\rangle$ at the conduction band, the intrinsic absorption spectrum $S_{\text{intrinsic}}$ is defined as:

$$S_{\text{intrinsic}} = \sum_n \int \delta[E_{\eta_n} - E]\Omega(|j_n\rangle)\Omega(|i_n\rangle)\alpha_{\text{intrinsic}}S(E)\mathrm{d}E \quad (1)$$

where $E_{\eta n}$ is the energy of η_n, $\Omega(|i_n\rangle)$ is the density of states of $|i_n\rangle$, $S(E)$ is the spectrum of the absorbed photon, and $\alpha_{\text{intrinsic}}$ is a constant scaling factor. The $S_{\text{intrinsic}}$ of ABO are depicted in Fig. 6.

2.2.2 Free-carrier absorption. Free-carrier absorption originates from transitions in a single band, in contrast to the intrinsic transitions from interband transitions. Transitions in the same band occur only if the band is partially occupied. Let η_m be an interband transition. $|i_m\rangle$ and $|j_m\rangle$ are respectively the initial state and final state of η_m. Phonons are emitted or absorbed during η_m to maintain the conservation of momentum. The transition probability decreases exponentially when the number of phonons involved in the transition increases.[3,14,15] The free-carrier absorption spectrum S_{FC} is defined as:

$$S_{\text{FC}} = \sum_m \int \delta[E_{\eta_m} - E]\Omega(|j_m\rangle)\Omega(|i_m\rangle)\alpha_{\text{FC}}\mathrm{e}^{-|k_{jm}-k_{im}|/\overline{k_{\text{phonon}}}}S(E)\mathrm{d}E \quad (2)$$

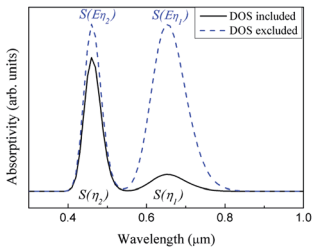

Fig. 6 Infrared spectra of the intrinsic absorption of ABO.

where k_{jm} is the momentum of the state $|j_m\rangle$ and $\overline{k_{\text{phonon}}}$ is the average momentum of the phonons. Five interband transitions were observed to influence the free-carrier absorption of ABO, and the S_{FC} of ABO is depicted in Fig. 7.

2.2.3 Lattice absorption. Lattice absorption consists of molecular vibrational absorption and phonon absorption. Various molecular vibrational modes of different frequencies exist in a lattice. Moreover, a vibrational mode of frequency f_{vib} can absorb photons of the same frequency if the electric dipole moment varies with the vibration. Change in the electric dipole moment caused by the vibrational mode shown in Fig. 3(1) can be obtained by the following steps:

(1) The electric dipole moment of the original molecular structure is calculated and marked as P_{original}.

(2) The molecular structure is then modified by taking the eigenvector of the vibrational mode as a perturbation (Fig. 8).

(3) Finally, the electric dipole moment of the modified molecular structure is calculated and marked as P_{modified}. The change in the electric dipole moment is the difference between P_{original} and P_{modified}.

The molecular vibrational absorption spectrum S_{vib} is defined as:

$$S_{\text{vib}} = \sum_i \int \delta[E_i - E]\Delta P_i\alpha_{\text{vib}}S(E)\mathrm{d}E, \quad (3)$$

where E_i and ΔP_i are the eigenvalue of the dynamic matrix and the change in the electric dipole moment of the i-th vibrational mode, respectively. The S_{vib} of ABO caused by the two vibrational modes are shown in Fig. 9. The absorptivity of $S_{\text{vib}}(1)$ is greater than that of $S_{\text{vib}}(2)$, since the change in the electric dipole moment ΔP_1 is greater than ΔP_2.

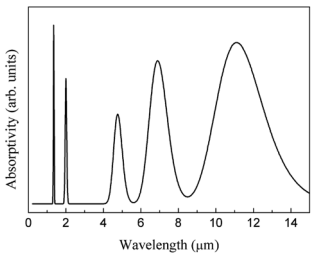

Fig. 7 Infrared spectrum of the free-carrier absorption of ABO.

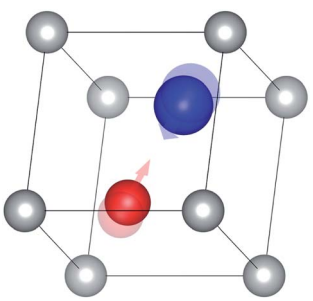

Fig. 8 Molecular structure modified by the eigenvector of the vibrational mode shown in Fig. 3(1); the transparent atoms indicate their original positions.

Open Access Article. Published on 24 August 2022. Downloaded on 1/31/2026 1:38:06 AM.
This article is licensed under a Creative Commons Attribution-NonCommercial 3.0 Unported Licence.

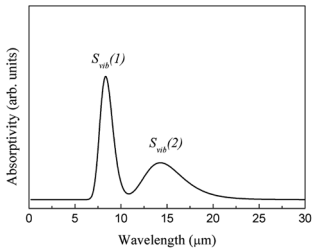

Fig. 9 Infrared spectrum of the molecular vibrational absorption of ABO.

The phonon band structure of a lattice consists of multiple branches. A phonon of frequency f_{phonon} on a transverse optical branch can absorb a photon of the same frequency. The phonon absorption spectrum S_{phonon} can be defined as follows:

$$S_{\text{phonon}} = \iint \delta\left[E_{\text{phonon}}(f) - E\right] \alpha_{\text{phonon}} S(E) \mathrm{d}E \Omega(f) \mathrm{d}f. \quad (4)$$

The integral over possible frequencies of phonons can be calculated, where $\Omega(f)$ is the phonon density of states with frequency f. The S_{phonon} of ABO is depicted in Fig. 10.

A combined infrared spectrum of ABO was then obtained through the summation of previous results (Fig. 6–10) Fig. 11.

3 Results and discussion

3.1 CeO_2 infrared spectra

3.1.1 Structural optimization. The molecular structure of CeO_2 was optimized by VASP using a conjugate gradient algorithm until the norms of all forces were lower than 0.015 eV Å^{-1}. For the calculations, Monkhorst–Pack special k-Points were selected when a k-mesh size of 5 × 5 × 5 was used in the full Brillouin zone. The optimized molecular structure is shown in Fig. 12. The lattice parameters of CeO_2 are $a = b = c = 3.834$ Å and $\alpha = \beta = \gamma = 60°$.

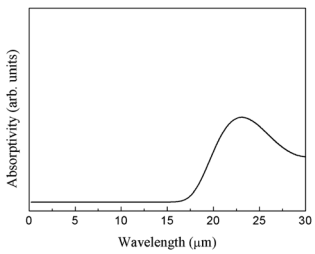

Fig. 10 Infrared spectrum of the phonon absorption of ABO.

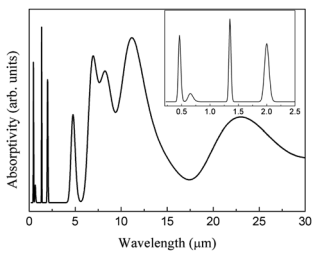

Fig. 11 Theoretical ABO infrared spectrum.

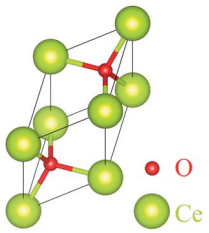

Fig. 12 Optimized molecular structure of CeO_2.

3.1.2 Conventional DFT results of CeO_2. The band structure and the density of states of CeO_2 were calculated based on the optimized molecular structure with a convergence criterion of energy change less than 10^{-8} eV between the two electronic self-consistent field (SCF) steps. The DOS and the band structure of CeO_2 are depicted in Fig. 13. The arrows in the band structure indicate the possible direct transitions between critical points.

The molecular vibrational modes of CeO_2 were calculated when the width of the displacement of each ion was set as ±0.02 Å. Finite differences were used to calculate the second derivatives and Hessian matrix (Table 1).

The phonon properties of CeO_2 were calculated using a 4 × 4 × 2 supercell. The cut-off energy for the plane-wave basis set was 500 eV, the convergence criterion for SCF energy was 10^{-8} eV, and a Monkhorst–Pack k-mesh size of 5 × 5 × 5 was used in the full Brillouin zone. The phonon density of states and phonon band structure are shown in Fig. 14.

3.1.3 Theoretical infrared spectra of CeO_2. The intrinsic absorption infrared spectrum was calculated using eqn (1) (Fig. 15).

Similarly, the free-carrier absorption infrared spectrum was calculated using eqn (2) (Fig. 16).

Changes in the electric dipole moment of different molecular vibrational modes are listed in Table 2.

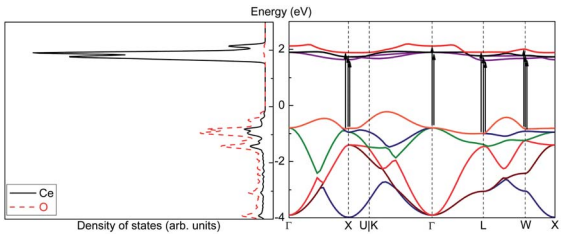

Fig. 13 Density of states (left) and band structure (right) of CeO_2.

Table 1 Molecular vibrational modes of CeO_2

Vibrational mode	1	2	3	4	5	6
Wavenumber (cm^{-1})	435.57	435.36	435.35	275.29	275.03	275.00

© 2022 The Author(s). Published by the Royal Society of Chemistry

Open Access Article. Published on 24 August 2022. Downloaded on 1/31/2026 1:38:06 AM.
This article is licensed under a Creative Commons Attribution-NonCommercial 3.0 Unported Licence.

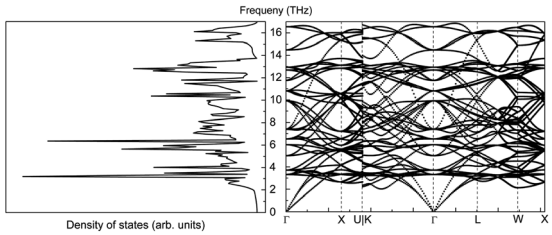

Fig. 14 Phonon density of states (left) and phonon band structure (right) of CeO_2.

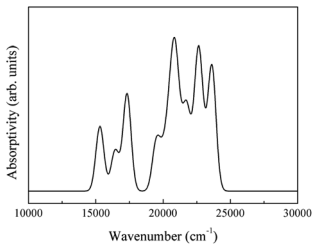

Fig. 15 Infrared spectrum of the intrinsic absorption of CeO_2.

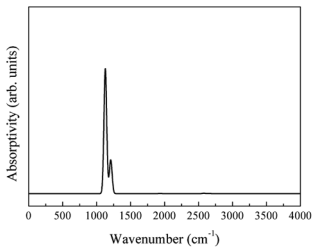

Fig. 16 Infrared spectrum of the free-carrier absorption of CeO_2.

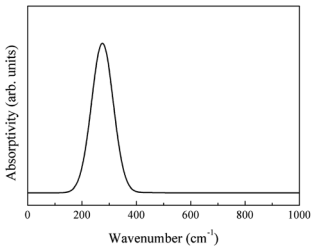

Fig. 17 Infrared spectrum of the molecular vibrational absorption of CeO_2.

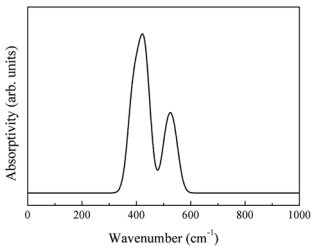

Fig. 18 Infrared spectrum of the phonon absorption of CeO_2.

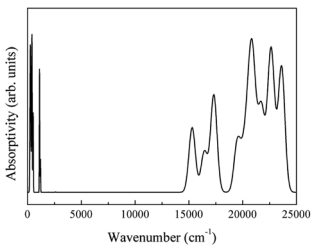

Fig. 19 Theoretical infrared spectra of CeO_2.

The molecular vibrational absorption infrared spectrum was calculated using eqn (3) (Fig. 17).

The phonon absorption infrared spectrum was calculated using eqn (4) (Fig. 18).

The theoretical CeO_2 infrared spectrum is depicted in Fig. 19.

The spectra obtained from calculations and an experimental report are shown in Fig. 20.[16]

The theoretical spectrum is in good agreement with the reported spectrum. The infrared absorption peaks of CeO_2 are located at 450 cm^{-1} and near cm^{-1} (Fig. 20(a)). The peak near 1200 cm^{-1} splits and a smaller branch with a higher frequency appears. The shapes of peaks are similar to those found in Fig. 20(b), with the peak near 1200 cm^{-1} shifting by about 200 cm^{-1}. An obvious difference between the spectra is the broad absorption peak at 3425 cm^{-1} (Fig. 20(b)). This absorption peak can be ascribed to the O–H group from impurities during synthesis.[16] It is not within the scope of this work to include the infrared dependence of impurities, thus the absence of the peak at 3525 cm^{-1} was not analyzed further. The experimental absorption properties can be obtained by broadening and shifting the peaks near 1200 cm^{-1} towards higher frequencies (Fig. 20(a)). Our calculations present the experimental infrared spectra of CeO_2 with accuracy.

3.2 Infrared spectra of $LaAlO_3$

3.2.1 Structural optimization. The molecular structure of $LaAlO_3$ was optimized by VASP using a conjugate gradient algorithm until the norms of all forces were lower than 0.02 eV

Table 2 Changes in the electric dipole moment of the molecular vibrational modes of CeO_2

Vibrational mode	1	2	3	4	5	6
Wavenumber (cm^{-1})	435.57	435.36	435.35	275.29	275.03	275.00
Change in the electric dipole moment (arb. units)	0.004	0.006	0.004	2.460	2.458	2.461

Open Access Article. Published on 24 August 2022. Downloaded on 1/31/2026 1:38:06 AM.
This article is licensed under a Creative Commons Attribution-NonCommercial 3.0 Unported Licence.

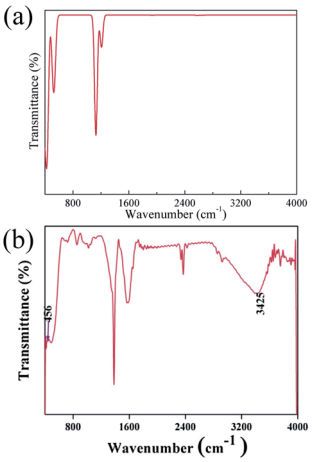

Fig. 20 (a) Theoretical infrared spectrum of CeO_2 and (b) experimental infrared spectrum of CeO_2 cited from ref. 16 with permission.

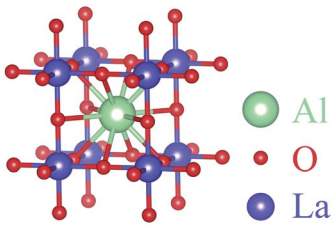

Fig. 21 Optimized molecular structure of $LaAlO_3$.

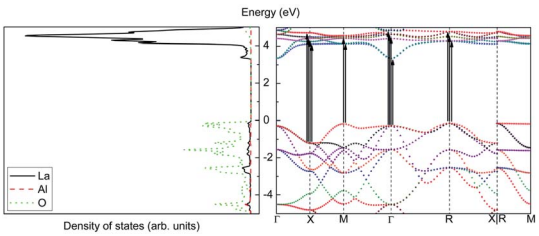

Fig. 22 Density of states (left) and band structure (right) of $LaAlO_3$.

$Å^{-1}$. For the calculations, Monkhorst–Pack special *k*-Points were selected when a *k*-mesh size of 7 × 7 × 7 was used in the full Brillouin zone. The optimized structure is shown in Fig. 21. The lattice parameters of $LaAlO_3$ are $a = b = c = 3.783$ Å and $\alpha = \beta = \gamma = 90°$.

3.2.2 Conventional DFT results of $LaAlO_3$. The density of states and band structure of $LaAlO_3$ were calculated based on the optimized structure with a convergence criterion of energy change less than 10^{-8} eV between the two electronic SCF steps. The density of states and band structure of $LaAlO_3$ are depicted in Fig. 22.

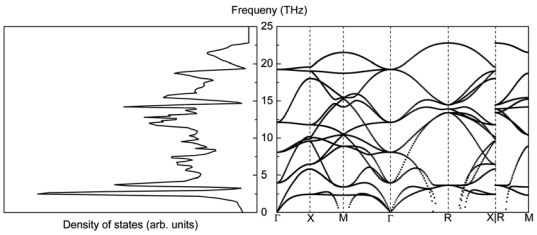

Fig. 23 Phonon density of states (left) and phonon band structure (right) of $LaAlO_3$.

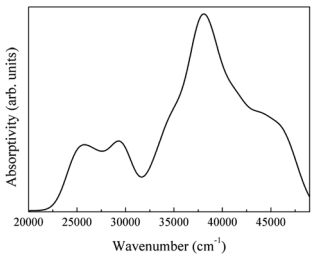

Fig. 24 Infrared spectrum of the intrinsic absorption of $LaAlO_3$.

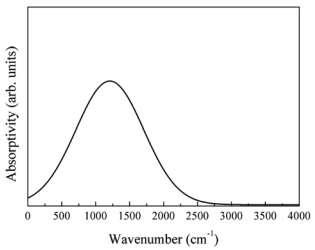

Fig. 25 Infrared spectrum of the free-carrier absorption of $LaAlO_3$.

The molecular vibrational modes of $LaAlO_3$ were calculated with the same procedure as for CeO_2 (Table 3).

The phonon properties of $LaAlO_3$ were calculated for a 2 × 2 × 2 supercell and a 3 × 3 × 3 Monkhorst–Pack *k*-mesh. The phonon density of states and phonon structure are depicted in Fig. 23.

3.2.3 Theoretical infrared spectra of $LaAlO_3$. The spectrum of intrinsic absorption $S_{intrinsic}$ was calculated using eqn (1) (Fig. 24).

The free-carrier absorption of $LaAlO_3$ originates from the highest valence band. The spectrum of the free-carrier absorption S_{FC} was calculated using eqn (2) (Fig. 25).

Changes in the electric dipole moment (ΔP) of different molecular vibrational modes of $LaAlO_3$ are listed in Table 4.

The molecular vibrational absorption spectrum S_{vib} was calculated using eqn (3) (Fig. 26).

Table 3 Molecular vibrational modes of $LaAlO_3$

Vibrational mode	1	2	3	4	5	6	7	8	9	10	11	12
Wavenumber (cm^{-1})	645.98	645.95	645.84	401.87	401.85	401.77	271.39	271.31	271.11	133.14	133.12	132.84

© 2022 The Author(s). Published by the Royal Society of Chemistry

Open Access Article. Published on 24 August 2022. Downloaded on 1/31/2026 1:38:06 AM.
This article is licensed under a Creative Commons Attribution-NonCommercial 3.0 Unported Licence.

Table 4 Changes in the electric dipole moment of the vibrational modes of $LaAlO_3$

Vibrational mode	1	2	3	4	5	6	7	8	9	10	11	12
Wavenumber (cm^{-1})	645.98	645.95	645.84	401.87	401.85	401.77	271.39	271.31	271.11	133.14	133.12	132.84
ΔP (arb. units)	11.507	11.507	11.507	0.183	0.183	0.183	0	0	0	9.339	9.339	9.339

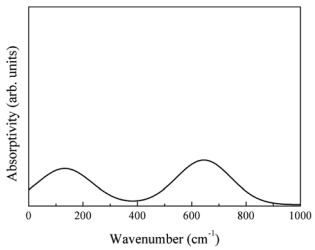

Fig. 26 Infrared spectrum of the molecular vibrational absorption of $LaAlO_3$.

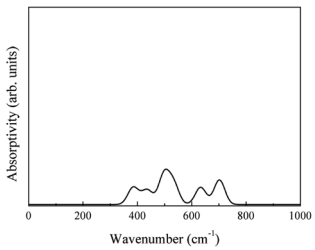

Fig. 27 Infrared spectrum of the phonon absorption of $LaAlO_3$.

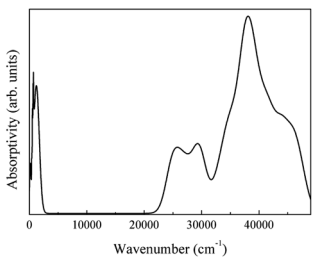

Fig. 28 Theoretical spectra of $LaAlO_3$.

The phonon absorption spectrum S_{phonon} was calculated by eqn (4) (Fig. 27).

Finally, the complete theoretical $LaAlO_3$ spectrum is presented in Fig. 28.

The calculated and experimental infrared spectra of $LaAlO_3$ are shown in Fig. 29.[17]

The theoretical spectrum is in good agreement with the reported spectrum. The absorptivity is high at 0.3 μm and 4–14 μm. The absorptivity decreases slightly when the wavelength is 14 μm. The spectrum shown in Fig. 29(b) can be reproduced by broadening the absorption peaks observed in Fig. 29(a). Overall, the experimental infrared properties of $LaAlO_3$ were in good agreement with our calculations.

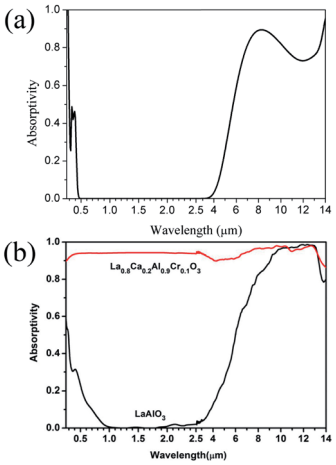

Fig. 29 (a) Theoretical infrared spectra of $LaAlO_3$ and (b) experimental infrared spectra of $LaAlO_3$ cited from ref. 17 with permission.

4 Conclusion

In this study, we have used a new theoretical method to predict quantitatively the infrared spectra of oxide crystals with high accuracy.

First, the principles and derivations of the method were shown, with a hypothetical oxide crystal ABO used as an example. Conventional DFT calculations were applied in the analysis of ABO, revealing properties including the electronic band structure, electronic DOS, molecular vibrational modes, phonon band structure, and phonon DOS would be provided. Based on these properties, our calculations predicted the spectra caused by basic mechanisms including intrinsic absorption, free-carrier absorption, molecular vibrational absorption, and phonon absorption. Intrinsic absorption was determined by the interband transitions of electrons; free-carrier absorption was determined by the transitions of electrons in one partially occupied band, in which phonons are involved; molecular vibrational absorption was determined by the vibrational modes changing the electric dipole moments; phonon absorption was determined by phonons on the transverse optical branches. The theoretical infrared spectra of ABO were presented through the summation of the spectra of different mechanisms.

The method was verified by comparing the theoretical and experimental CeO_2 and $LaAlO_3$ spectra. The theoretical spectra of CeO_2 successfully reproduced the experimental spectra, with similar shapes in the characteristic absorption peaks at 450 and 1200 cm^{-1}. Two differences hindered the accuracy of our method. At 1200 cm^{-1}, the frequency of the absorption peak in the theoretical spectrum differs from the peak in the

Open Access Article. Published on 24 August 2022. Downloaded on 1/31/2026 1:38:06 AM.
This article is licensed under a Creative Commons Attribution-NonCommercial 3.0 Unported Licence.

experimental spectrum by nearly 200 cm^{-1} and was ascribed to a mathematical error in the first-principles calculations. The absorption peak in the experimental spectrum at 3425 cm^{-1}, which was likely caused by impurities during synthesis, is absent in the theoretical spectrum. For $LaAlO_3$, the theoretical and experimental spectra are in good agreement. Moreover, both the thin absorptivity peak at 0.3 μm and the broad absorptivity peak at 4–14 μm are similar. In all, the method successfully provided a rapid and accurate preview of the infrared spectra of oxide crystals.

This method sheds light on the theoretical investigation of the infrared properties of oxide crystals. The only initial requirement for our method is the molecular structure of the oxide crystal. Theoretical spectra that are in good agreement with the experimental results can then be provided. Applying this method in the initial assessment of materials will reduce the cost of numerous experiments, improving the efficiency of material screening.

There are still problems with this method. Even though the characteristic CeO_2 and $LaAlO_3$ peaks are accounted for in the theoretical spectra, the exact positions of these peaks differ slightly from the experimental peaks. The method works well for CeO_2 and $LaAlO_3$, whose unit cells are both small and simple but is less accurate in predicting the peaks for larger complex oxide crystals. Future studies aim to solve these problems. The equations used in this methodology would account for more complex models to carry out the mechanisms more precisely. Different calculation conditions and exchange functionals in the DFT calculations will be tested to improve the accuracy of the proposed method. The ignored parts in the analyses of basic mechanisms, such as the exciton absorption and indirect interband transitions, will be reintroduced to provide more detailed results. The improved method aims to be more accurate and practicable for future studies.

Author contributions

Guangpu Luo: conceptualization, data curation, formal analysis, investigation, methodology, resources, software, validation, visualization, and writing – original draft. Wenyue Zhao: methodology and software. Hongbo Guo: conceptualization, funding acquisition, project administration, supervision, validation, and writing – review & editing. Shengkai Gong: conceptualization, funding acquisition, project administration, supervision, validation, and writing – review & editing.

Conflicts of interest

The authors declare that they have no known competing financial interests or personal relationships that could have appeared to influence the work reported in this paper.

Acknowledgements

This research has been sponsored by Science Center for Gas Turbine Project (P2021-A-IV-001-003) and the National Natural Science Foundations of China no. 52101117. The high performance computing resources at Beihang University is also acknowledged for providing supercomputing time. The authors would like to thank TopEdit (**https://www.topeditsci.com**) for its linguistic assistance during the preparation of this manuscript.

References

1 P. Hohenberg and W. Kohn, *Phys. Rev.*, 1964, **136**, B864–B871.
2 W. Kohn and L. J. Sham, *Phys. Rev.*, 1965, **140**, A1133–A1138.
3 K. Huang and R. Q. Han, *Solid State Physics*, Higher Education Press, Beijing, 1st edn, 1991.
4 G. Kresse and J. Hafner, *Phys. Rev. B: Condens. Matter Mater. Phys.*, 1993, **47**, 558–561.
5 G. Kresse and J. Furthmüller, *Comput. Mater. Sci.*, 1996, **6**, 15–50.
6 G. Kresse and J. Furthmüller, *Phys. Rev. B: Condens. Matter Mater. Phys.*, 1996, **54**, 11169–11186.
7 V. Wang, N. Xu, J.-C. Liu, G. Tang and W.-T. Geng, *Comput. Phys. Commun.*, 2021, **267**, 108033.
8 Y. Hinuma, G. Pizzi, Y. Kumagai, F. Oba and I. Tanaka, *Comput. Mater. Sci.*, 2017, **128**, 140–184.
9 G. Kresse and J. Hafner, *J. Phys.: Condens. Matter*, 1994, **6**, 8245–8257.
10 G. Kresse and D. Joubert, *Phys. Rev. B: Condens. Matter Mater. Phys.*, 1999, **59**, 1758–1775.
11 J. P. Perdew, K. Burke and M. Ernzerhof, *Phys. Rev. Lett.*, 1996, **77**, 3865–3868.
12 A. Togo and I. Tanaka, *Scr. Mater.*, 2015, **108**, 1–5.
13 J. Neugebauer and T. Hickel, *Wiley Interdiscip. Rev.: Comput. Mol. Sci.*, 2013, **3**, 438–448.
14 M. J. Weber, *Phys. Rev.*, 1968, **171**, 283–291.
15 L. A. Riseberg and H. W. Moos, *Phys. Rev.*, 1968, **174**, 429–438.
16 P. Latha, P. Kasirajan and S. Karuthapandian, *Optik*, 2017, **154**, 242–250.
17 Z. Han, X. Li, J. Ye, L. Kang, Y. Chen, J. Li and Z. Lin, *J. Am. Ceram. Soc.*, 2015, **98**, 2336–2339.

© 2022 The Author(s). Published by the Royal Society of Chemistry